Corrosion Science 239 (2024) 112410

Contents lists available at ScienceDirect

Corrosion Science

journal homepage: www.elsevier.com/locate/corsci

Corrosion behavior of laser powder bed fusion manufactured nickel-free stainless steels in high-temperature water

Sneha Goel [a], Martin Bojinov [b], Jan Capek [c], Timo Saario [a], Efthymios Polatidis [d], Tuomas Kantonen [e], Antti Salminen [e], Malte Blankenburg [f], Ashish Ganvir [e], Zaiqing Que [a,*]

[a] Advanced Materials for Nuclear Energy, VTT Technical Research Centre of Finland, Espoo 02150, Finland
[b] Department of Physical Chemistry, University of Chemical Technology and Metallurgy, Sofia 1756, Bulgaria
[c] Laboratory for Neutron Scattering and Imaging (LNS), Paul Scherrer Institute, Villigen 5232, Switzerland
[d] Laboratory of Technology & Strength of Materials (LTSM), Department of Mechanical Engineering & Aeronautics, University of Patras, Patras 26504, Greece
[e] Department of Mechanical and Materials Engineering, University of Turku, Turku 20520, Finland
[f] DESY Photon Science, Deutsches Elektronen-Synchrotron, Hamburg 22607, Germany

ARTICLE INFO

Keywords:
Additive manufacturing
Nickel-free steel
Laser Powder Bed Fusion
Heat treatment
Corrosion
High-temperature water

ABSTRACT

The paper presents a comprehensive investigation of electrochemical behavior of laser powder bed fusion (PBF-LB/M) nickel-free stainless steels in high-temperature water. The PBF-LB/M nickel-free steels processed with various laser parameters and heat treatments exhibit tunable microstructures. Electrochemical impedance spectroscopy (EIS) indicates a 2–3 times lower oxidation rate for the nickel-free steels compared to wrought 316 L. The outer layer crystallites on nickel-free steels are close to pure Fe oxides. The significantly lower concentration of Ni in the inner oxide and at the alloy/oxide interface account for the important variations of the parameters of water reduction/hydrogen oxidation reactions than wrought 316 L.

1. Introduction

The rapidly growing field of additive manufacturing (AM) has transformed the production industry, and a crucial component of Industry 4.0 is focusing on digital fabrication. Laser powder bed fusion (PBF-LB/M) is one of the most promising and versatile metal AM techniques successfully used to process a wide range of materials. It utilizes high-power lasers to melt the raw material added layer-by-layer, allowing for the fabrication of intricate engineering components with complex shapes. Its unique capabilities have sparked interest across a wide range of applications, from aerospace and automotive industries to biomedical and energy sectors [1].

Along with revolutionizing growth of AM, there is an increasing concern regarding the use of nickel in various alloys, particularly in austenitic stainless steels. Austenitic stainless steels are iron-based alloys which are corrosion resistant, thanks to the relatively high Cr content, and they are categorized by compositions; some commonly used austenitic stainless-steel varieties include 316 L and 304 L. Nickel is predominantly used in austenitic stainless steels, because of its strong austenite stabilization capabilities, its impact on the mechanical behavior and corrosion resistance at high temperatures. However, environmental footprint associated with nickel extraction and processing has raised sustainability concerns [2]. Additionally, nickel is known to cause allergic reactions in a significant part of the population [3]. As a result, there has been growing interest in nickel-free alloys as alternatives to traditional stainless steels [4]. These alloys do not only reduce the risk of allergic reactions but also align with global efforts to adopt environmentally responsible materials and manufacturing processes [5]. Alternative austenite stabilizers have been identified, through introduction of increased nitrogen and manganese as alloying elements in Ni-free stainless steels [6–11] that strengthen the material and influence the resistance to corrosion. Nitrogen and manganese can stabilize austenitic structure, which is accompanied by good creep performance, high ductility, relatively high strength and good resistance to corrosion at the same time.

Nickel-free steels produced by PBF-LB/M have garnered attention for their unique microstructures, which can be tailored to optimize desired properties, including corrosion resistance and magnetic behavior [12,13]. There have been attempts to apply nickel-free stainless steels in chemical industry and biomedical fields. Nevertheless, despite their potential, a comprehensive understanding of the corrosion behavior of PBF-LB/M nickel-free steels in demanding environments (*e.g.*,

* Corresponding author.
E-mail address: zaiqing.que@vtt.fi (Z. Que).

https://doi.org/10.1016/j.corsci.2024.112410
Received 14 May 2024; Received in revised form 20 August 2024; Accepted 23 August 2024
Available online 24 August 2024

Table 1
Chemical compositions (wt%) of the used Ni-free steel powder, and nuclear grade stainless steel 316 L for comparison.

Material	Fe	Cr	Ni	Mn	Mo	Si	N	O	C	Co	S	P	Nb
PANACEA powder	Bal.	17.3	0.1	11.4	3.24	0.7	0.177	0.156	0.028	0.01	0.005	0.017	0.01
316 L [21]	Bal.	17.3	11.5	1.8	2.6	0.37	0.05	0.026	0.027	0.01	0.004	0.03	0.01

Table 2
The PBF-LB/M processing parameters of the investigated material conditions. The notations p, s, h, d and VED represent power, scanning speed, hatch distance, layer thickness and volumetric energy density, respectively.

PBF-LB/M parameters	Low VED	Medium VED	High VED
p (W)	140	160	300
s (mm s^{-1})	1000	600	400
h (mm)	0.08	0.08	0.08
d (mm)	0.03	0.03	0.03
VED (J mm^{-3})	58.3	111.1	312.5

high-temperature water, aggressive chemical media, *etc.*) is lacking. There have been reports on corrosion of nickel-free steels in neutral chloride solutions at ambient temperature only [14–17]. Concerning AM produced materials, studies in high-temperature, high-pressure aqueous electrolytes have been focused on nickel-containing stainless steels [18, 19].

High-temperature water media are encountered in critical applications such as nuclear reactors, steam turbines, and other power generation systems. In these conditions, materials must exhibit excellent corrosion resistance to ensure long-term operational integrity and safety. PBF-LB/M nickel-free steels, if proven to be corrosion-resistant in such aggressive conditions, could find extensive use and contribute to enhanced efficiency in high-temperature water-based applications.

In that context, the present paper aims to address the knowledge gap by investigating the corrosion behavior of PBF-LB/M nickel-free steel in a high-temperature water environment (at 288 °C). In-situ electrochemical measurements, microstructural evolution investigations and post-mortem characterizations of as-built and post heat-treated PBF-LB/M nickel-free stainless steels produced by various printing parameters have been performed and analyzed. Based on the experimental and calculation results, preliminary conclusions on the compatibility of AM nickel-free steels are drawn.

2. Experimental

2.1. Material, PBF-LB/M process, and heat treatment

The feedstock used for PBF-LB/M processing was a Ni-free stainless-steel powder commercially available from Sandvik AB (Sweden). The virgin powder used in this study was completely ferritic with an average particle size of 27.5 μm. The Particle Size Distribution (PSD) for the applied powder can be found in supplement Figure S1. The chemical composition of the powder is provided in Table 1. Higher Mn and N contents compared to traditional AISI 316 L stainless steel are used to stabilize the austenite structure. The tap density and relative density of the powder was 4.8 $g{\cdot}cm^{-3}$ and 7.75 $g{\cdot}cm^{-3}$, respectively.

The specimens were printed using an Aconity MIDI+ PBF-LB/M machine (Aconity3d, Germany). A single mode, continuous wave, infrared laser with a wavelength of 1070 μm was employed. The details of printing can be found in the supplement. Three volumetric energy densities (VEDs) were chosen to achieve different starting microstructures. A summary of printing parameters is given in Table 2. Post isothermal heat treatment (HT) at 900 °C for 30 min followed by water quenching was employed for all three materials. Higher temperature was used for faster kinetics of austenite formation [20]. The investigated samples were marked as Low VED, Low VED_HT, Medium VED, Medium VED_HT, High VED, and High VED_HT, the suffix HT indicating heat-treated materials.

2.2. Electrochemical measurements

Specimens (0.6 × 0.6 × 0.3 cm) with a final surface finish of 0.25 μm were employed for high-temperature electrochemical experiments. A Nickel wire was spot welded to the lateral aspect of the specimens for electrochemical measurement purposes. The electrochemical measurements were conducted within a wrought AISI 316 L stainless steel autoclave integrated into a recirculating loop. All the surface of the specimens was exposed to the coolant except for the wire which was sealed with multi-layer PTFE tape. The flow rate in the autoclave is low enough so that the influence of the edges was minimal. The exposed environment is a simulated pressurized water reactor (PWR) coolant, *i.e.,* 35 cm^3 H_2 / kg H_2O, 1000 ppm B (as H_3BO_3) and 2.2 ppm Li (as LiOH) with a $pH_{288°C}$ of 7.0. A nickel/nickel oxide couple pH electrode served as reference, and all potentials are re-calculated to the standard hydrogen electrode (SHE) scale. Electrochemical measurements were carried out with an Ivium Compactstat. Current-time curves were registered during steps from –0.8 V (0.5 s) to –0.55 V (8 s). Cyclic voltammetry was measured in the interval –0.815 / 0.30 / –0.815 V with a sweep rate of 1 mV s^{-1}. The reproducibility of current transients was better than ±5 %. Potential values were adjusted by subtracting the IR drop estimated as the product of the measured current density and the ohmic resistance calculated from high-frequency intercept of impedance spectra. Electrochemical impedance spectroscopy (EIS) was measured after 50–120 h of exposure at the corrosion potential (ca. –0.77 V_{SHE}) in the frequency range from 10^5 Hz to 10^{-3} Hz with an ac amplitude of 50 mV (rms). In the frequency range 1 kHz to 100 kHz, spurious time constants due to the interaction between electrodes in the poorly conducting medium are usually observed, so this frequency range was not used for analysis. The reproducibility of the impedance spectra was better than ±2 % by magnitude and ±3° by phase angle. Linearity was checked by demonstrating that spectra measured with amplitudes from 20 to 50 mV were identical within the reproducibility limit, and causality verified by Kramers-Kronig compatibility test embedded in ZView analysis software.

2.3. Microstructural characterization

Microstructural characterization of as-prepared and heat-treated samples prior and after high-temperature water exposure was performed using a Zeiss Crossbeam 540 scanning electron microscope (SEM) with an EDAX Hikari Plus electron backscatter diffraction (EBSD) detector. Electron channeling contrast imaging (ECCI) was conducted with the solid-state four-quadrant backscatter detector. The parameters for backscattered electrons (BSE) imaging were set at 15 keV and 1.5 nA, with a working distance (WD) of 5–8 mm. For EBSD analysis, the WD was set to 11–14 mm, employing a step size of 100 nm. Inversed pole figure (IPF), phase map and kernel average misorientation (KAM) map were analyzed based on EBSD data. The Energy-dispersive X-ray spectroscopy (EDS) was acquired with a Zeiss ULTRA 55 SEM equipped with EDAX Hikari Camera Oxford EDS-detector operated at 5 keV with a 120 μm aperture. The EDS raw data was post processed using homemade scripts in Wolfram Mathematica.

Synchrotron X-Ray diffraction was measured at P21.2 Swedish Materials Science Beamline at DESY Photon Science. TS1500 furnace was mounted at the sample position and the sample was heated at the rate 50 °C/min up to 900 °C where the sample was hold for 2 hours. The X-

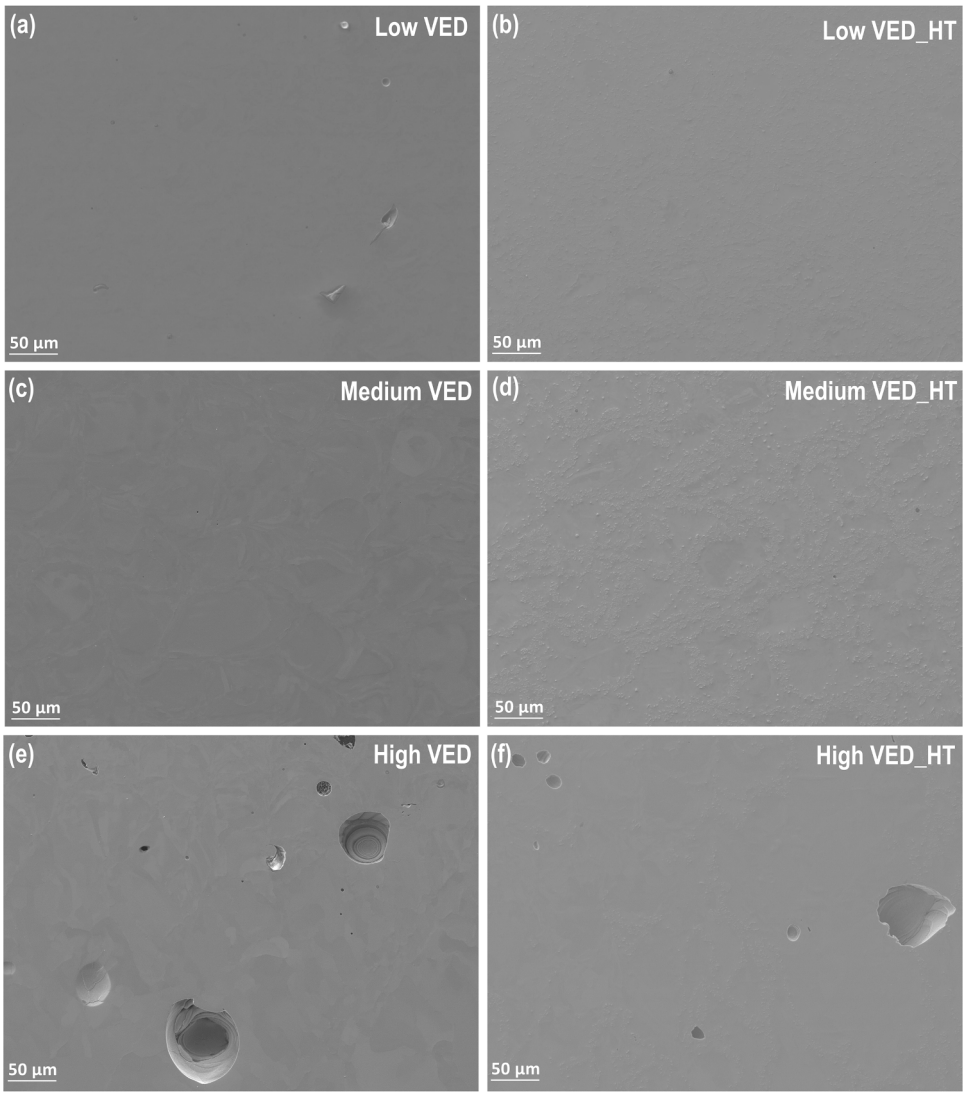

Fig. 1. SEM images of (a) Low VED, (b) Low VED_HT, (c) Medium VED, (d) Medium VED_HT, (e) High VED and (f) High VED_HT samples.

Ray diffraction experiment was performed in the transmission mode using 4 VAREX XRD4343CT area at 85 keV with a beam spot-size of 500 × 500 µm^2. The energy of the beam (85 keV) corresponds to a wavelength of about 0.1459 Å. During annealing, diffraction measurements were carried out with a 5-s acquisition time for each diffraction pattern and a 15-s break between each acquisition. Calibration of the diffraction setup was performed using a LaB6 NIST SRM 660b standard in conjunction with GSAS-II software. 2D diffraction images were integrated across the full azimuthal range, followed by Rietveld refinement using GSAS-II. Following refinement of lattice parameters for the face centered cubic (FCC), body centered cubic (BCC) and Chi phases, phase fractions were recalculated. Afterwards, a cylindrical symmetry texture model with an 8th harmonic order for FCC and BCC phases, respectively, was applied for modeling the crystallographic structure. An isotropic microstrain model was employed to account for peak broadening in all phases, while the background signal was fitted using a 6th-order Chebyshev polynomial. Backward sequential refinements were conducted, progressing towards shorter annealing times, wherein phases, texture, microstrain models, and hydrostatic/elastic strains were refined to capture evolving lattice parameters due to chemical segregation. The maximum refinement cycles were limited to 10, with refined parameter sets propagated to subsequent histograms. The goodness indicators of all phases were sufficiently high and the acquired phase fraction data exhibits rather low uncertainty.

Table 3
Summary of microhardness of the PBF-LB/M specimens with different VEDs before and after HT.

Specimen condition	Microhardness HV1
Low VED	386 ±8
Low VED_HT	289 ±7
Medium VED	354 ±17
Medium VED_HT	271 ±7
High VED	278 ±25
High VED_HT	244 ±7
Reference 316 L	152 ± 4

10–15 Vickers micro-hardness measurements with 1 kg load (HV1) were performed using Struers DuraScan-80 device on each material condition. All microstructure images shown have a build direction out of plane.

3. Results

3.1. Microstructure and hardness properties

Porosity was analyzed from the SEM images taken on the as-polished samples, as shown in Fig. 1. High VED results in high porosity with some

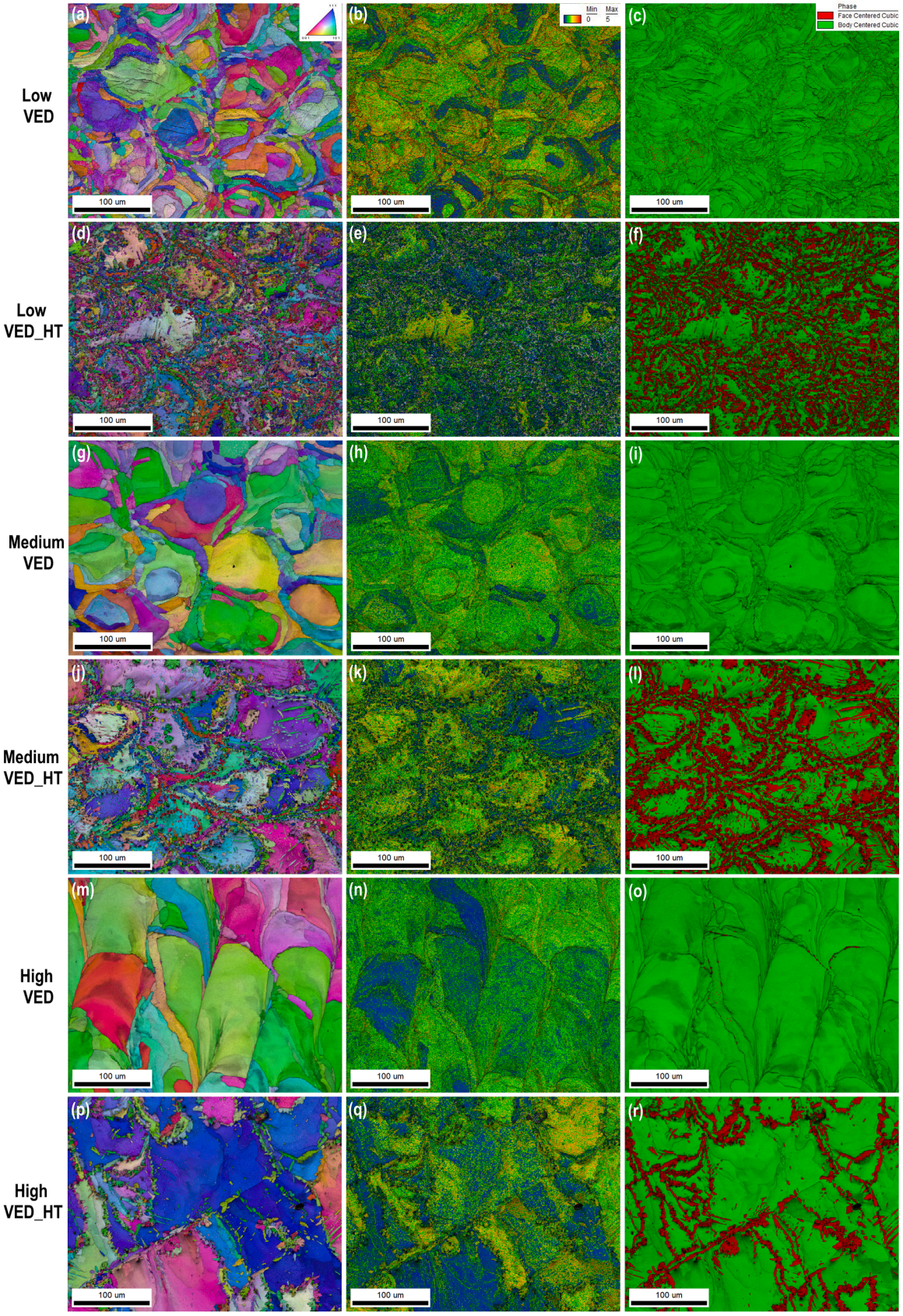

Fig. 2. EBSD maps of (a-c) Low VED, (d-f) Low VED_HT, (g-i) Medium VED, (j-l) Medium VED_HT, (m-o) High VED and (p-r) High VED_HT samples. (a, d, g, j, m, p) IPF maps, (b, e, h, k, n, q) KAM maps and (c, f, i, l, o, r) phase maps.

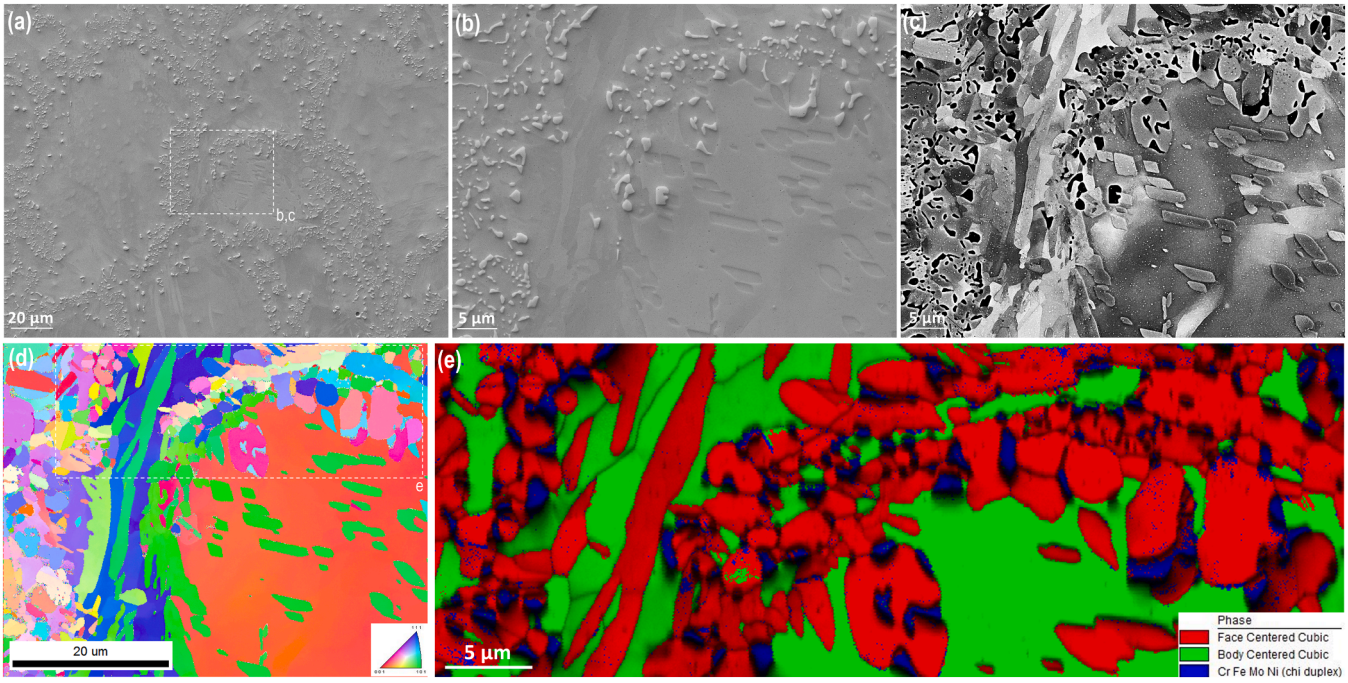

Fig. 3. (a-b) SEM secondary electron images, (c) SEM backscattered electron image, (d) EBSD IPF map and (e) phase map of Medium VED_HT sample.

lack of fusion defects as evidenced in Fig. 1(e). Medium VED seems to be the optimum one, as spherical pores were rarely observed after this type of treatment. The measured density for the investigated materials is 7.71, 7.68 and 7.56 g cm^{-3} for Low VED, Medium VED and High VED, respectively. A summary of the hardness of investigated specimens is presented in Table 3. In general, samples printed with higher VED exhibit lower hardness. The hardness also decreases after HT. Moreover, the nickel-free steels show much higher hardness values than the reference AISI 316 L, even after HT.

EBSD maps are collected in Fig. 2. IPF images show that the columnar-shaped grain size increases with VED. The average grain sizes of low, medium and high VED specimens are around 50, 80 and 120 µm, respectively. The geometrically necessary dislocation (GND) density decreases with increasing VED, as revealed from the KAM maps. Bimodal grain structures were observed in the heat-treated samples, the coarse grains being surrounded by fine ones, indicating a potential recrystallization occurring during the HT. These fine grains were austenitic FCC phase formed at the grain boundaries of BCC grains during HT.

With high-magnification characterization (Fig. 3), a third phase, Chi duplex, can be found in the heat-treated specimens. The Chi duplex phase normally precipitates either at the grain boundaries of FCC grains or the interface between FCC and BCC phases (Fig. 3(e)). Detailed EBSD phase maps containing FCC, BCC and Chi duplex phases of Low VED_HT, Medium VED_HT and High VED_HT samples can be found in supplement Figure S2.

The ECCI images showing the microstructure of the investigated materials are shown in Fig. 4. The decrease of GND density with increasing VED that is revealed from the KAM maps was confirmed by ECCI Fig. 4(a, c, e). After HT, the dislocation density significantly reduced and stacking faults were observed, particularly in the Low VED_HT specimen, which has the highest amount and largest size of stacking faults among the heat-treated specimens. The High VED_HT sample has the smallest amount of stacking faults and the largest number of dislocations in the heat-treated specimens.

The weight fractions of FCC, BCC and Chi duplex phases in Low VED, Medium VED and High VED specimens upon heating according to synchrotron X-ray diffraction can be deduced from Fig. 5. Exemplary synchrotron diffraction pattern and integrated line profile can be found in supplement Figure S3. With the increase of annealing time at 900 °C, there is an increase of the portions of FCC and Chi duplex phases, which saturated after around 1 h. The beam was down during the annealing for High VED sample, thus no values after an annealing time of 30 minutes at 900 °C were obtained but only at the end of the measurement. Therefore, only a boundary value can be provided for the High VED sample. Nevertheless, the data show that the percentage of FCC and Chi duplex phases decreased with the increase of VED. The summary of phase fractions of BCC, FCC and Chi duplex for each specimen is presented in Table 4.

The chemical composition (wt%) of the FCC, BCC and Chi duplex phases in Ni-free stainless-steel HT specimens are shown in Table 5. The Chi duplex phase is enriched in Mo, Fe and Si compared to BCC and FCC phases. The FCC phase is enriched in Mn and N while containing lower amounts of Cr and Si compared to the BCC phase. The detailed quantified EDS area maps and spectra can be found in supplement Figure S4. The accuracy of the chemical composition of each phase is confirmed by the coherence between phase maps based on EBSD and the elemental maps from EDS, as illustrated in supplement Figure S5.

3.2. *High-temperature electrochemical behavior*

3.2.1. *Voltammetric and current-time measurements*

A comparison of linear sweep voltammograms for the investigated steels is shown in Fig. 6(a). The current densities are comparable, but the highest for High VED_HT and the lowest for the Medium VED_HT steels, respectively. Several regions can be discerned in the curves, indicating transformations of the surface oxides. An attempt at rationalizing these regions is made by constructing the *E-pH* diagram of the Fe-Cr-Mn-H_2O system at 288 °C using HSC 6.0 software (Outokumpu Ltd.). The main standout point of this diagram as depicted in Fig. 6(b) is the absence of the very large stability region of $NiFe_2O_4$ (the main component of the outer oxide layer crystals on nickel-containing stainless steels [22–24]), which is replaced by a rather narrow region of the corresponding manganese-iron oxide $MnFe_2O_4$, due to the very low Ni content of the steels subject to the present investigation.

Tafel plots of the data in the range –0.85/–0.6 V are shown in Fig. 6

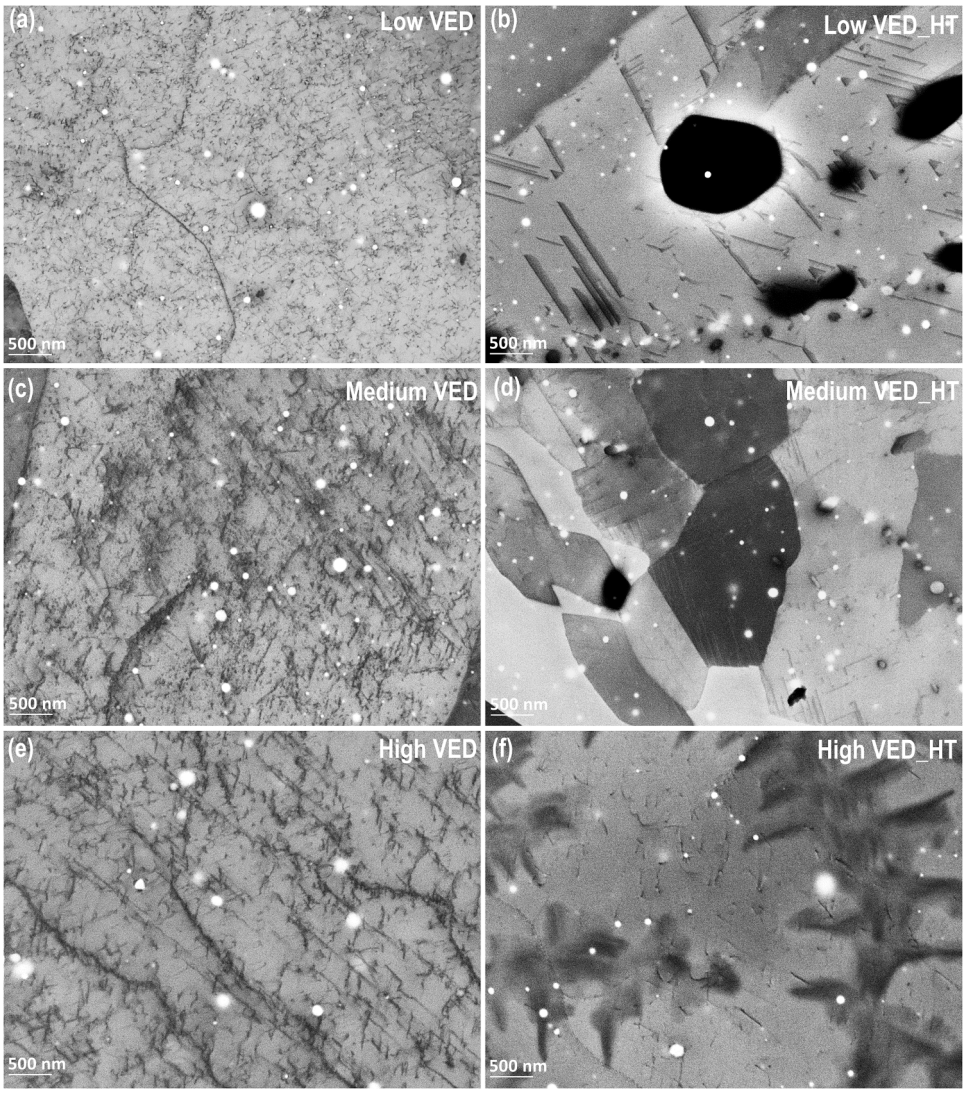

Fig. 4. ECCI images of (a) Low VED, (b) Low VED_HT, (c) Medium VED, (d) Medium VED_HT, (e) High VED and (f) High VED_HT samples.

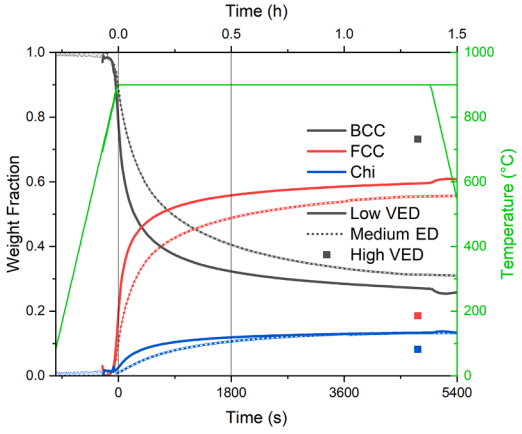

Fig. 5. Weight fraction of FCC, BCC and Chi duplex phases in Low VED, Medium VED and High VED specimens upon heating at 900 °C according to X-ray diffraction.

(c). To obtain estimates of the transfer coefficients and corrosion current of the rate-determining anodic and cathodic reactions, the acquired curves were subjected to fitting procedures according to the Stern-Geary equation [25]:

$$i = i_{corr}\left[e^{b_a(E-E_{corr})} - e^{-b_c(E-E_{corr})}\right] \quad (1)$$

where E_{corr} is the corrosion potential, i_{corr} – the corrosion current

Table 4
Summary of FCC phase percentage in the studied materials after 30 min at 900 °C according to the X-ray diffraction analysis.

	Low VED_HT	Medium VED_HT	High VED_HT
BCC, %	32.3	40.6	> 73.2
FCC, %	55.8	48.8	< 18.6
Chi duplex, %	11.9	10.6	< 8.2

Table 5
Chemical composition (wt%) of the FCC, BCC and Chi duplex phases in Ni-free stainless-steel HT specimens identified by quantified EDS area maps.

Material	Fe	Cr	Ni	Mn	Mo	Si	N	O
FCC	Bal.	17.78	0.39	9.47	1.97	0.5	0.32	0.82
BCC	Bal.	21.2	0.37	7.52	2.96	0.61	0.14	0.77
Chi duplex	Bal.	21.25	0.33	7.21	12.71	0.77	0.16	0.87

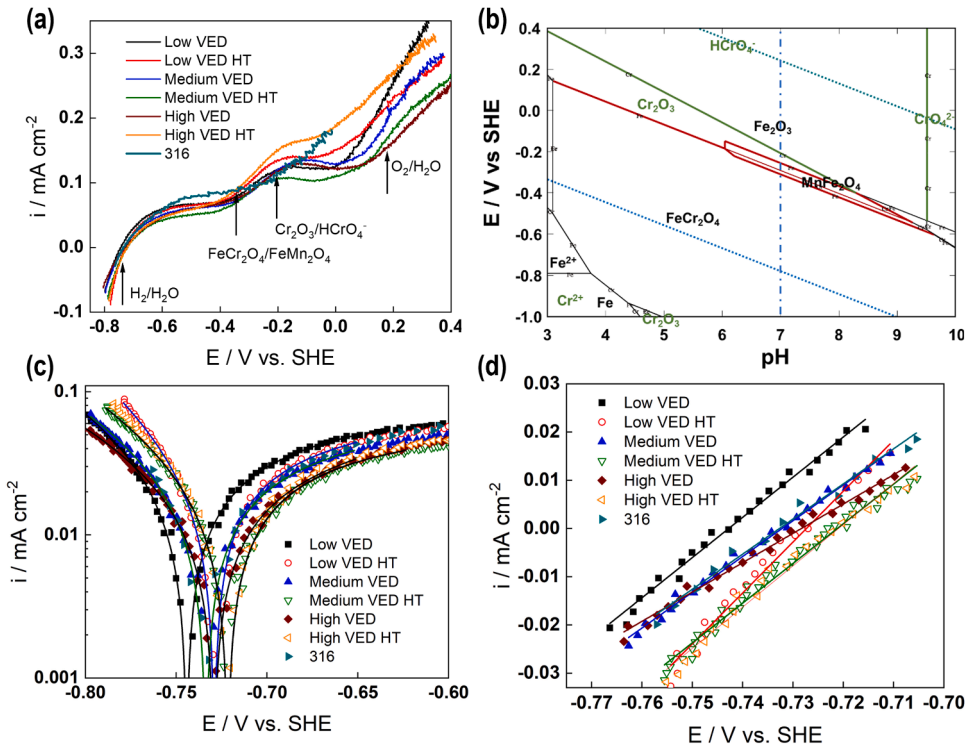

Fig. 6. (a) Linear sweep voltammograms of the studied materials, E - pH diagram of the Fe-Cr-Mn-H_2O system at 288 °C (total Fe 0.1 μmol kg^{-1}, total Cr 0.01 μmol kg^{-1}, total Mn 0.5 μmol kg^{-1}), (c) Tafel plots in the range of potentials –0.8/–0.6 V, and (d) linear parts of the voltammograms in the vicinity of the corrosion potential.

Table 6
Electrochemical parameters calculated from the current-potential curves and current-time transients.

Material	i_{corr} / mA cm^{-2}	b_a / V^{-1}	b_c / V^{-1}	R_p / kΩ cm^2 (Tafel)	R_p / kΩ cm^2 (from *i-E*)	*cBV* / mC cm^{-2}
Low VED	0.053	1.93	14.2	1.16	1.20	0.016
Low VED_HT	0.042	2.74	21.1	1.01	0.95	0.014
Medium VED	0.048	1.8	13.1	1.41	1.35	0.014
Medium VED_HT	0.040	1.8	15.3	1.45	1.31	0.020
High VED	0.037	3.6	11.6	1.78	1.64	0.013
High VED_HT	0.045	1.1	14.5	1.44	1.49	0.016
Reference 316 L [21]	0.051	3.2	15.3	1.37	1.34	0.016

density, and $b_{i\ (i=a,c)} = \alpha_i(nF/RT)$ – the exponential coefficients of the anodic and cathodic coupled reactions.

The resulting best-fit curves, depicted by solid lines, indicate satisfactory agreement between the model and the experimental data in the vicinity of the corrosion potential. The derived values of the exponential coefficients of the anodic and cathodic reactions (b_a and b_c) and the corrosion current density (i_{corr}) are collected in Table 6 together with an estimated value of the polarization resistance $R_p = [i_{corr}(b_a + b_c)]^{-1}$. The polarization resistance was also extracted from the slopes of the current-potential curves at the vicinity of the corrosion potential (±0.03 V), Fig. 6(d), and the estimates obtained with both methods agree reasonably with each other. It is noteworthy to mention that the parameters extracted from the analysis of *i-E* curves do not differ significantly between materials, *i.e.,* the rate-limiting step of the overall corrosion reaction is probably similar.

Re-passivation data are plotted in Fig. 7 in log(*i*) - reciprocal charge (Q^{-1}) coordinates, which allows an estimation of the characteristic parameter (*cBV*) based on the high-field repassivation model [26] expressed by the equation:

$$\log i(t) = \log A + \frac{cBV}{Q(t)} \quad (2)$$

where *V* is the potential drop in the oxide film, while *A* and *B* are the parameters related to the activation energy for ion migration through it. $c = zF/2.3\ V_m$, where *z* is the number of transferred electrons during oxidation and V_m is the molar volume of the oxide. The *cBV* values for different steels are also collected in Table 6. It can be stated that also re-passivation rates of the investigated materials as indicated by *cBV* are roughly similar. It is also worth mentioning that the high-field model gives at best an approximate fit to the data, and a refinement of the model by adding film dissolution reaction during repassivation could improve the fitting. Such a refinement will be attempted in the near future.

3.2.2. *EIS measurements*

Various electrochemical processes within a system typically exhibit distinct time constants required to attain a steady state when responding to sinusoidal voltage perturbation. The larger time constant, the lower characteristic frequency in the impedance spectrum. Hence, an overview of the electrochemically detectable processes and their respective roles regarding electrochemical response can be obtained by conducting EIS across a wide frequency range (e.g., 10^4 to 10^{-4} Hz). Corrosion behavior linked to the system's polarization resistance is typically governed by the electrochemical processes prevalent at the lower frequency range ($\leq 10^{-3}$ Hz).

The EIS data shown in *Fig. 8* indicate that all studied nickel-free steels behave very similarly. The overall polarization resistance (inversely proportional to the corrosion rate) can be estimated from the low-frequency end of the impedance magnitude (|Z|) vs. frequency plots. As a preliminary conclusion (before modeling), Medium VED_HT and High VED steels exhibit higher impedance magnitude at 10^{-3} Hz, and therefore lower corrosion rate than the rest of the specimens. The

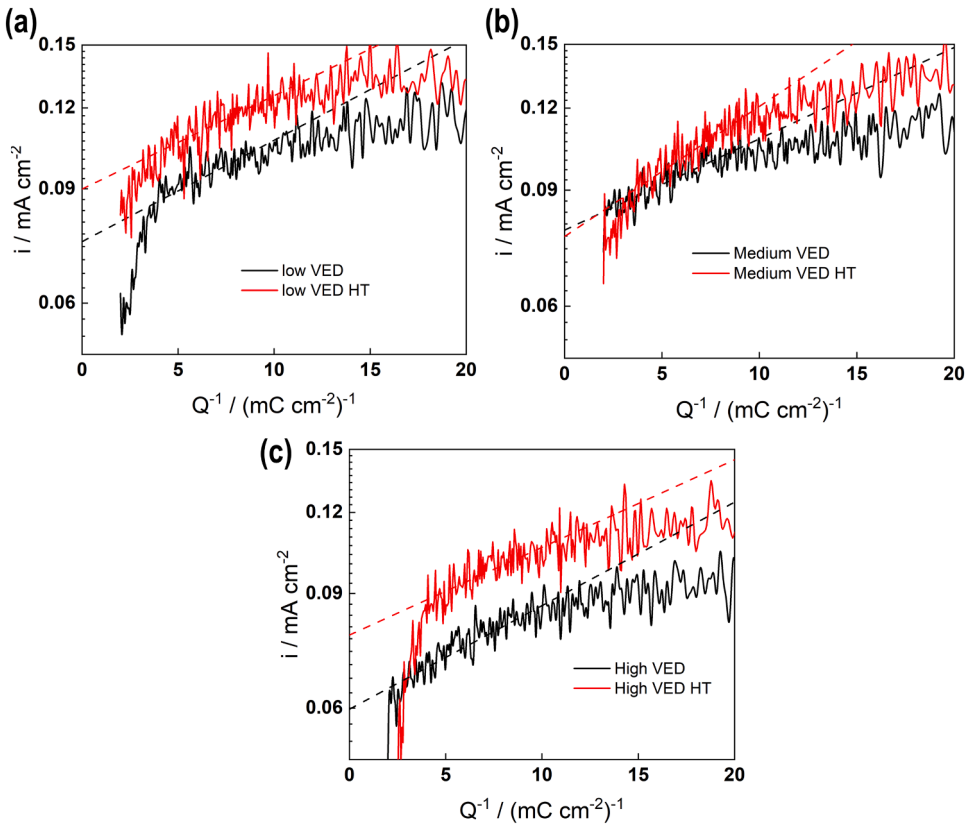

Fig. 7. Check of the high-field model of repassivation for the studied materials. (a) Low VED and Low VED_HT, (b) Medium VED and Medium VED_HT, (c) High VED and High VED_HT samples.

polarization resistance of the reference 316 L material is, however, 3–4 times lower than those of the nickel-free alloys, indicating a much higher corrosion rate. It is also important to mention that the polarization resistances estimated from voltammetric data are in general lower than those from EIS and no appreciable difference between values for the Ni-free steels and reference 316 L is detected from voltammetric data. This illustrates the higher diagnostic power of impedance method in comparison to conventional voltammetric studies.

Through meticulous deconvolution of the EIS spectra, a total of four time constants can be discerned, as indicated by arrows in *Fig. 8* (b). The time constant at the lowest frequency is presumed to primarily reflect the transport of ionic defects through the semiconducting oxide, i.e., the barrier layer portion, of the oxide film. The two intermediate time constants correspond to the adsorption of intermediate products and charge transfer at the interface between the barrier layer and solution. At the higher frequency range, the time constant is linked to the electronic properties of the barrier layer.

The EIS data were analyzed utilizing the Mixed-Conduction Model (MCM) for quantifying the electrochemical response and corrosion behavior of the investigated steels (for a summary of model equations, see Appendix). The solid lines in Fig. 8 depict the best-fit results, showcasing that the model accurately captures both the frequency distribution and magnitude of the impedance spectrum ($R^2 > 0.975$, $\chi^2 < 0.01$). Estimates of the kinetic and transport parameters are presented in Table 7.

The rate constants of oxidation at the alloy/barrier layer interface are 2–3 times lower for the nickel-free steels in comparison to wrought AISI 316 L, and so are the diffusion coefficients of both oxygen and cations, the field strength in the barrier layer on Ni-free materials being ca. 50 % higher. In addition, barrier layer thicknesses on Ni-free materials are ca. 20 % lower than wrought AISI 316 L. These observations correlate well with the experimentally observed higher polarization resistances and accordingly lower oxidation and corrosion release rates of these steels when compared to the AISI 316 L. The differences in kinetic and transport parameters between individual nickel-free materials are comparatively small. The estimated rate constants of oxidation at the interface of alloy and oxide are the smallest for the Low VED_HT and Medium VED_HT, indicating that the corrosion rate of these two materials is somewhat lower. Important differences are noted in the parameters of the hydrogen reaction, which are probably related to the fact that practically no nickel (known to catalyze hydrogen oxidation) is available at the barrier layer/solution interface for such materials. The considerably larger values of the rate constants of interstitial cation ejection ($k_{2\,M}$) and oxygen vacancy filling ($k_{2\,O}$) at the film/solution interface for the nickel-free steels in comparison to the reference AISI 316 L material remain unexplained at this point and might be related to a different structure of the interface in the quasi-absence of nickel (or the presence of much larger concentration of Mn at that interface when compared to conventional austenitic steels).

3.3. Characterization of oxide layer

Fig. 9 presents the outer oxidized surfaces of the exposed steels. The outer oxide layers of the investigated Ni-free steel specimens possess similar morphology of sparse and randomly-distributed oxide particles, indicating similar transportation of ions through the oxide film. Conversely, large numbers of smaller particles are observed on the reference 316 L, *i.e.,* the structure and population of the outer layer on it is significantly different.

Cross-sectional characterization of the oxide films on studied alloys after exposure are shown in Figs. 10–12. Disperse and very thin oxide layers (less than ~200 nm) covered by sparse outer layer crystals were observed. Local in-depth composition estimated using EDS line scans is also shown in the figures. Both atomic and normalized cation

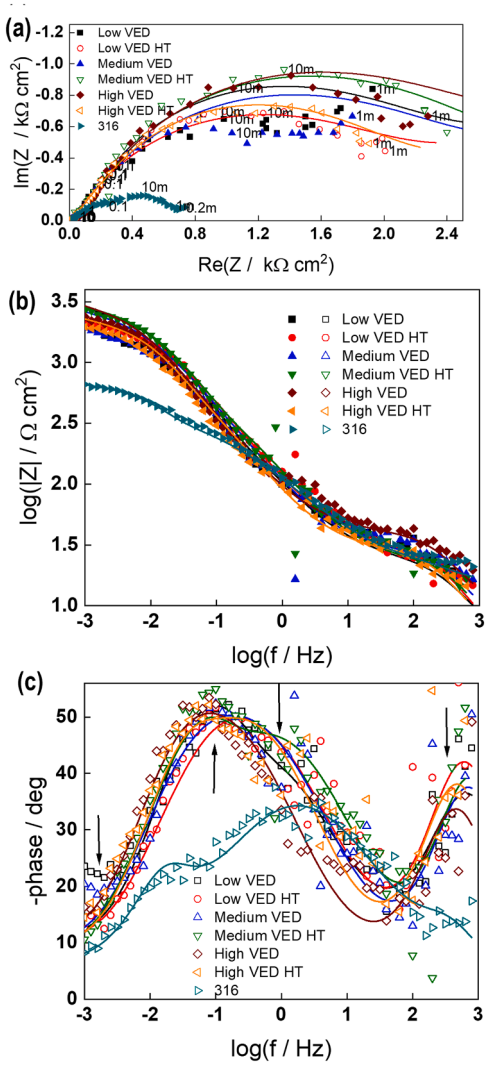

Fig. 8. EIS spectra of the studied steels after 50 h of exposure to the primary coolant in (a) complex plane (parameter is frequency in Hz), (b) impedance magnitude vs. frequency and (c) phase shift vs. frequency coordinates (time constants marked with arrows). Points – experimental data, solid lines – best-fit calculation.

concentrations vs. depth are presented. The interface between the oxide and substrate is estimated via sigmoidal regression of O (at%) and Fe (at %) profiles, whereas the boundary (barrier layer) between the outer layer crystal and the inner layer - via similar treatment of the normalized Fe and Cr profiles. The calculational results are summarized in Table 8.

The outer layer thickness is comparable to the dimensions of the respective crystallites observed at the surface (1.5–2.5 μm) in Fig. 9. In contrast to what is observed for type AISI 316 L steel on which nickel ferrite is formed [21], the outer layer is almost pure Fe oxide (presumably Fe_3O_4). This indicates that Mn is most probably preferentially dissolved in the PWR coolant (the Mn content in the outer crystallites is less than 3 %). The inner layer is considerably thinner than that on reference AISI 316 L steel and has a minimum thickness on the Low VED sample, the thickness on Medium VED and Medium VED_HT samples being the largest. Typically, the inner layer contains 15–20 % Cr and 10 % Mn, so its composition can be approximately expressed as $Cr_{0.6}Mn_{0.4}Fe_2O_4$. A small amount of Ni is evenly distributed in the outer and inner layers.

4. Discussion

4.1. Effect of printing parameters and heat treatment on microstructure

The microstructure of the Ni-free materials can be tunable with different printing parameters and after HTs. The as-built PBF-LB/M Ni-free specimens investigated in the present work exhibit a nearly 100 % ferritic microstructure. This can be explained by two factors: (a) chemical composition of the alloy, (b) the ultra-fast cooling rates during PBF-LB/M process. Previous work on high Cr/Ni ratio iron alloys has shown higher ferrite content with increasing cooling rate during solidification [27]. This is justified by their solidification with ferrite as the primary phase, and since the high cooling rates of the order of 10^4 °C/s limit solid state phase transformation to austenite. The cooling rates during PBF-LB/M processing are higher than 10^5 °C/s and the Cr/Ni ratio in the investigated Ni-free alloy was very high [28]. On the other hand, low cooling rates allow sufficient time for nucleation and growth of austenite from ferrite. The preferential heterogeneous nucleation sites for FCC austenite are regions with low Cr/Ni ratios, such as grain and cell boundaries. After HT of the fully ferritic matrix in the present study, the austenite grains nucleated and grew on the ferrite grain boundaries. The amount of austenite was higher in low and medium VED specimens compared to high VED specimen, which can be attributed to the larger grain boundary area in the former due to smaller grain sizes. Additionally, the chemical segregation could also facilitate the austenite formation. As shown in Table 5 and supplement Figure S2, the FCC phase is enriched in N and Mn while low in Cr and Si compared to the

Table 7
Summary of the parameters estimated by fitting EIS results to the MCM. The parameters of reference 316 L were obtained from [21].

Parameters	Low VED	Low VED_HT	Medium VED	Medium VED_HT	High VED	High VED_HT	Reference 316 L
10^{11} k_M /mol cm^{-2} s^{-1}	6.0	5.3	6.0	5.0	5.0	6.0	15
10^{11} k_O /mol cm^{-2} s^{-1}	4.5	4.3	4.3	3.1	3.0	4.0	10
C_{sc} / μF cm^{-2}	18.3	18.1	15.2	19.1	17.5	16.6	22
L / nm	55	55	55	61	45	52	78
10^8 D_e / cm^2 s^{-1}	5.3	6.6	4.3	5.5	2.2	1.8	5.0
R_t / Ω cm^2	18	21	19	16	21	19	2.8
$C_{F/S}$ / mF cm^{-2}	3.9	3.2	3.4	2.5	4.9	3.9	2.8
10^9 $k_{2\,M}$ / cm s^{-1}	13	13	13	15	17	15	4.5
10^9 $k_{2\,O}$ / cm s^{-1}	5.0	2.4	6.1	5.5	4.0	5.5	2.0
10^{10} $k_{1\,H}$ / mol cm^{-2} s^{-1}	2.3	2.3	2.2	1.5	2.2	1.5	1.1
10^{11} $k_{2\,H}$ / mol cm^{-2} s^{-1}	1.3	1.3	1.4	1.5	1.3	1.4	12
1011 k−1 H / mol cm−2 s−1	1.5	1.5	1.5	1.3	1.5	1.3	13
104 k−2 H / cm s−1	1.6	1.6	1.7	1.6	2.0	1.6	1.4
β / nmol cm^{-2}	1.0	1.0	0.5	0.4	1.0	0.7	4.9
10^{17} D_M / cm^2 s^{-1}	1.0	1.0	1.0	1.0	1.0	1.0	5.0
10^{17} D_O / cm^2 s^{-1}	0.20	0.20	0.20	0.20	0.20	0.20	4.0
$\vec{E}$ / kV cm^{-1}	150	150	140	150	150	90	109

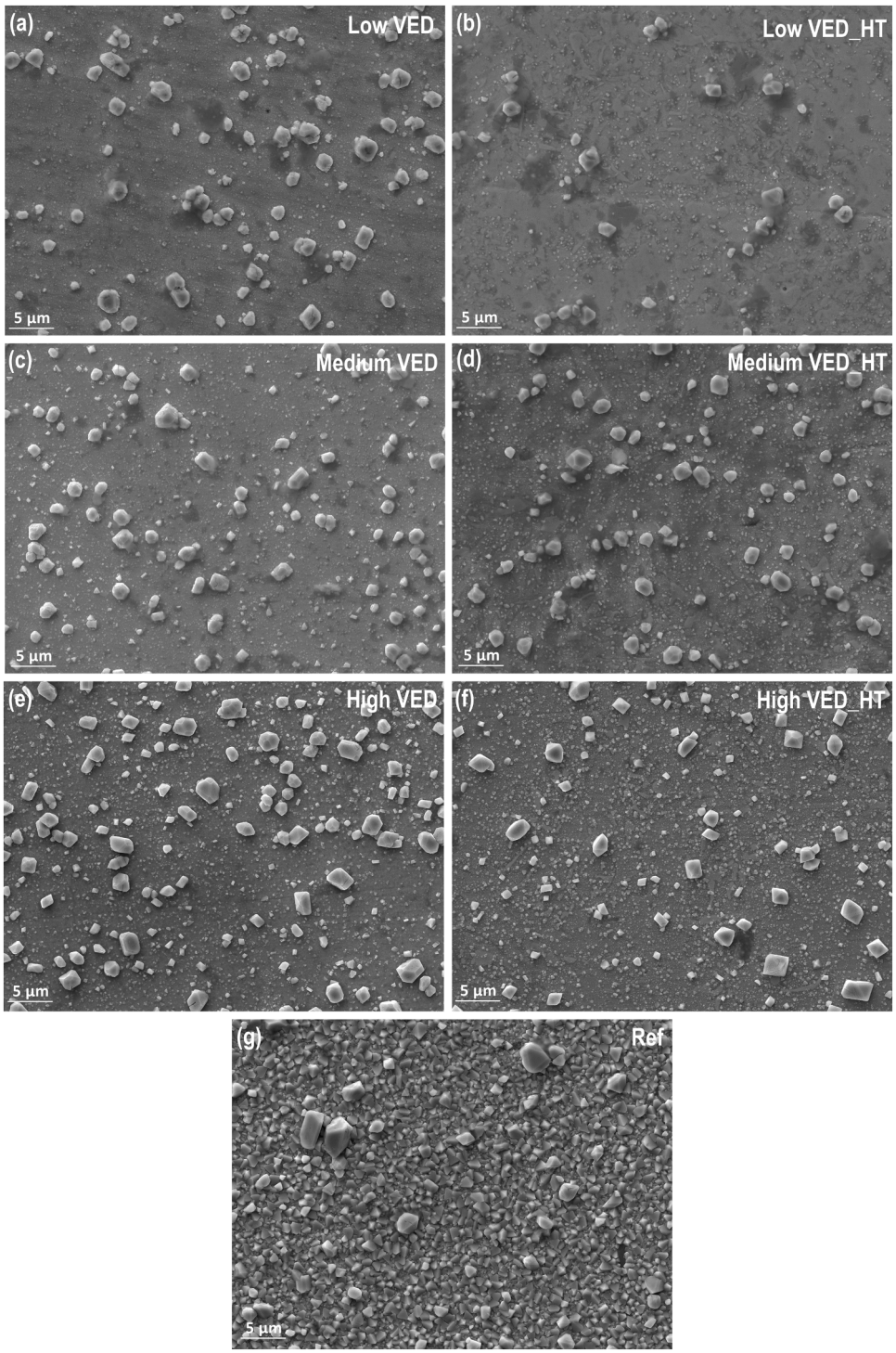

Fig. 9. Outer surfaces of studied steels after the exposure to the high-temperature environment. (a) Low VED, (b) Low VED_HT, (c) Medium VED, (d) Medium VED_HT, (e) High VED and (f) High VED_HT sample, (g) wrought 316 L reference.

BCC phase. For the chosen HT temperature of 900 °C the austenite phase could have possibly formed directly from the ferrite with no intermediate martensite formation [29].

The resultant hardness of the investigated specimens was an interplay of several factors such as relative fraction of austenite, ferrite, grain size [30] as well as the GNDs. Moreover, previous studies have shown that carbon content in the ferritic-austenitic dual phase steels can have significant impact on the relative hardness of austenite compared to ferrite. For a dual phase steel with similar Carbon content as the nickel-free steel used in this study, it has been found through nano- and micro-indentation hardness measurements that austenite exhibited higher hardness than the ferrite [31]. This is possibly explained by the higher work hardening rate of austenite compared to ferrite [32]. However, in another study on nanoindentation of such dual phase steel, the ferrite was found to be harder than the austenite [33]. Thus, there is contradiction in the reported observations in literature. Previous studies have also shown that mechanical behavior of even the same phase in different types of steels can exhibit variation owing to difference in material history, *i.e.,* HT, chemical composition, internal stress *etc.* [34]. In the present study, austenite formation upon HT was accompanied by

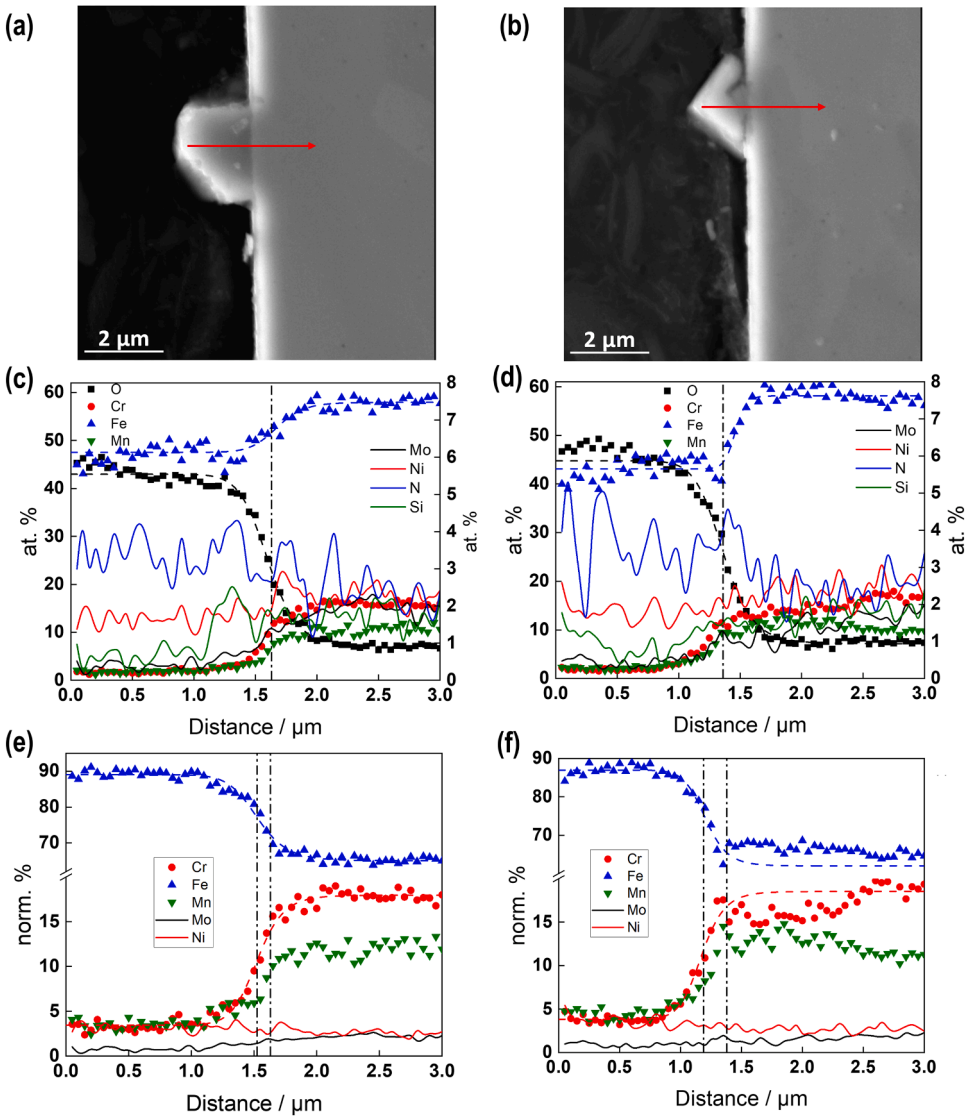

Fig. 10. (a, b) Cross-sectional SEM images (line scan directions are indicated with arrows) and (c-f) EDS line scan results for (a, c, e) Low VED and (b, d, f) Low VED_HT materials after exposure. (c, d) Atomic concentrations vs. depth, (e, f) normalized cation concentrations vs. depth. Vertical lines indicate the positions of oxide/alloy and outer/inner layer interfaces estimated by sigmoidal fits of depth profiles.

reduced hardness. Apart from the relative fraction of austenite and ferrite, the Chi duplex phase could impact the hardness as it can retard the movement of dislocations during plastic deformation. In PBF-LB/M processed as-built 316 L, Chen *et al.* [35] have found dislocation strengthening to have the largest contribution to strengthening and significantly more than grain boundary strengthening. The present observations are consistent with these earlier findings. KAM and ECCI analysis results provided in Fig. 2(c, f, i, l, o, r) and Fig. 4 demonstrate that dislocation density decrease with increasing VED as well as upon HT. Moreover, the grain size increase with VED causing even further drop in hardness [36].

4.2. Correlation of electrochemical behavior with microstructure

EIS measurements in high-temperature water at 288 °C and their modelling reveal a relatively similar electrochemical behavior of the investigated nickel-free steels, which is very different from that of reference AISI 316 L steel. It is worth noting that since all specimens in this study receive the same surface finish before electrochemical tests, thus the difference in corrosion behavior is mainly related to the matrix microstructure instead of the surface defects resulted from the printing process. Microstructural factors that might result in the change in electrochemical response are discussed here. Fig. 13 shows that the Chi duplex phase itself seem to be more resistant to oxidation and corrosion compared to FCC or BCC phases. The images in Fig. 13 were taken from locations where oxide film was peeled off from the surface during sample preparation. The black chi phase stands out, particularly in Fig. 13(b-c), which indicates the oxidation of the chi phase is less than the matrix. There is no evident difference in the oxidation behavior between FCC and BCC phases. The Chi duplex phase is enriched in Mo, Fe and Si compared to BCC and FCC phases. Compositional differences between the phases have a radical influence on the corrosion susceptibility of the phases. However, Chi duplex phase depletes the Mo from the surrounding matrix, which makes the interface between Chi duplex and other phases become more prone to corrosion. Generally, Chi duplex is an intermetallic phase which precipitates fast in the beginning and tends to transform into sigma phase after a prolonged aging [37]. Chi duplex phase is relatively brittle and it also creates chemical heterogeneities. It has been observed that the depletion of important alloying elements like Mo from the matrix towards the Chi duplex particles, makes the materials locally sensitive to corrosion [38].

The formation of an oxide film on stainless steel in high-temperature

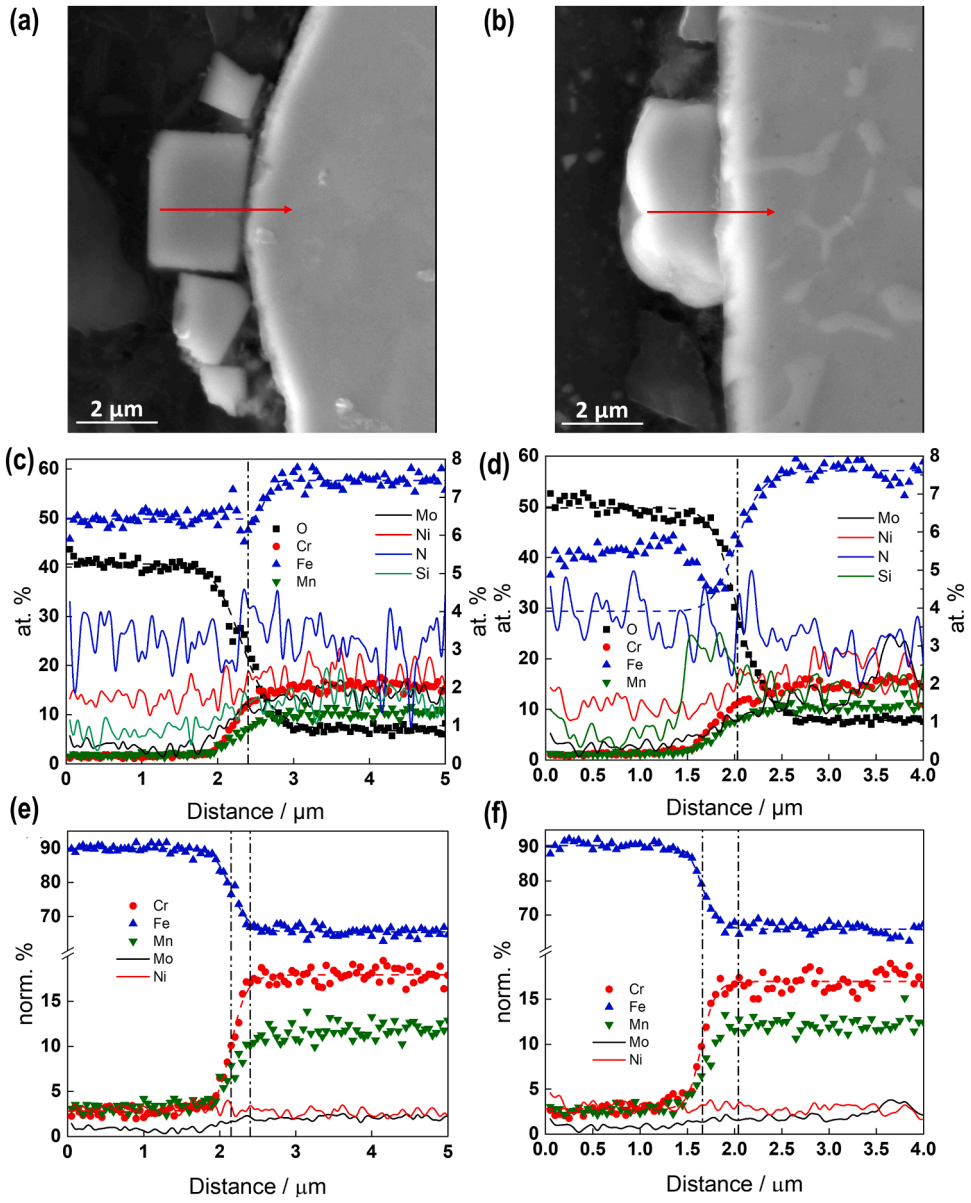

Fig. 11. (a, b) Cross-sectional SEM images (line scan directions are indicated with arrows) and (c-f) EDS line scan results for (a, c, e) Medium VED and (b, d, f) Medium VED_HT materials after exposure. (c, d) Atomic concentrations vs. depth, (e, f) normalized cation concentrations vs. depth. Vertical lines indicate the positions of oxide/alloy and outer/inner layer interfaces estimated by sigmoidal fits of depth profiles.

water environment is crucial in influencing their general and localized corrosion susceptibility [39–41]. The thickness of the inner layers on the nickel-free steels is considerably thinner than that on reference 316 L steel. As indicated by EIS modelling, the diffusion coefficient of electronic carriers within the oxide film, the field strength within the oxides and the parameters associated with the hydrogen evolution/oxidation reaction are comparable for the Ni-free steels investigated, differing significantly from those of the reference AISI 316 L steel. This reveals that ion and electron conduction mechanisms of the oxide layers in all investigated Ni-free steels are similar, but the quasi-absence of Ni and the presence of relatively large concentrations of Mn at the alloy/passive film interface led to important alteration of electrochemical process rates. Furthermore, the rate constants of alloy oxidation at the metal/-film interface and ejection of interstitial cations at the film/solution interface are lower for the Low and Medium VED_HT specimens. This indicates a decelerated process of oxide dissolution kinetics leading to reduced rates of oxidation and corrosion release from those steels, which are likely due to the higher phase fraction of Chi duplex in these specimens (Table 4). Moreover, the reduced capacitances observed in the space charge layer within the semiconducting oxide film of the PBF-LB/M nickel-free steel specimens in comparison to the AISI 316 L point to a lower number of electron donors and ionic defects in the passive layer. Therefore, the stability of the passive film formed on the PBF-LB/M nickel-free steels is better than that on the wrought counterpart in the studied high-temperature water environment.

4.3. *Application of Ni-free stainless steels in demanding environments*

The PBF-LB/M nickel-free steels exhibit tailored microstructures (HT, phase distribution, grain size, *etc.*) and hardness. The oxidation and corrosion release rates of the studied nickel free steels are found to be significantly lower than that of the wrought 316 L in simulated PWR environment. PBF-LB/M 316 L or 316 stainless steels have been applied in many demanding industries including automotive, aerospace and nuclear. Comparing to the electrochemical behaviors of PBF-LB/M 316 L in similar high-temperature water environments [21,42], the

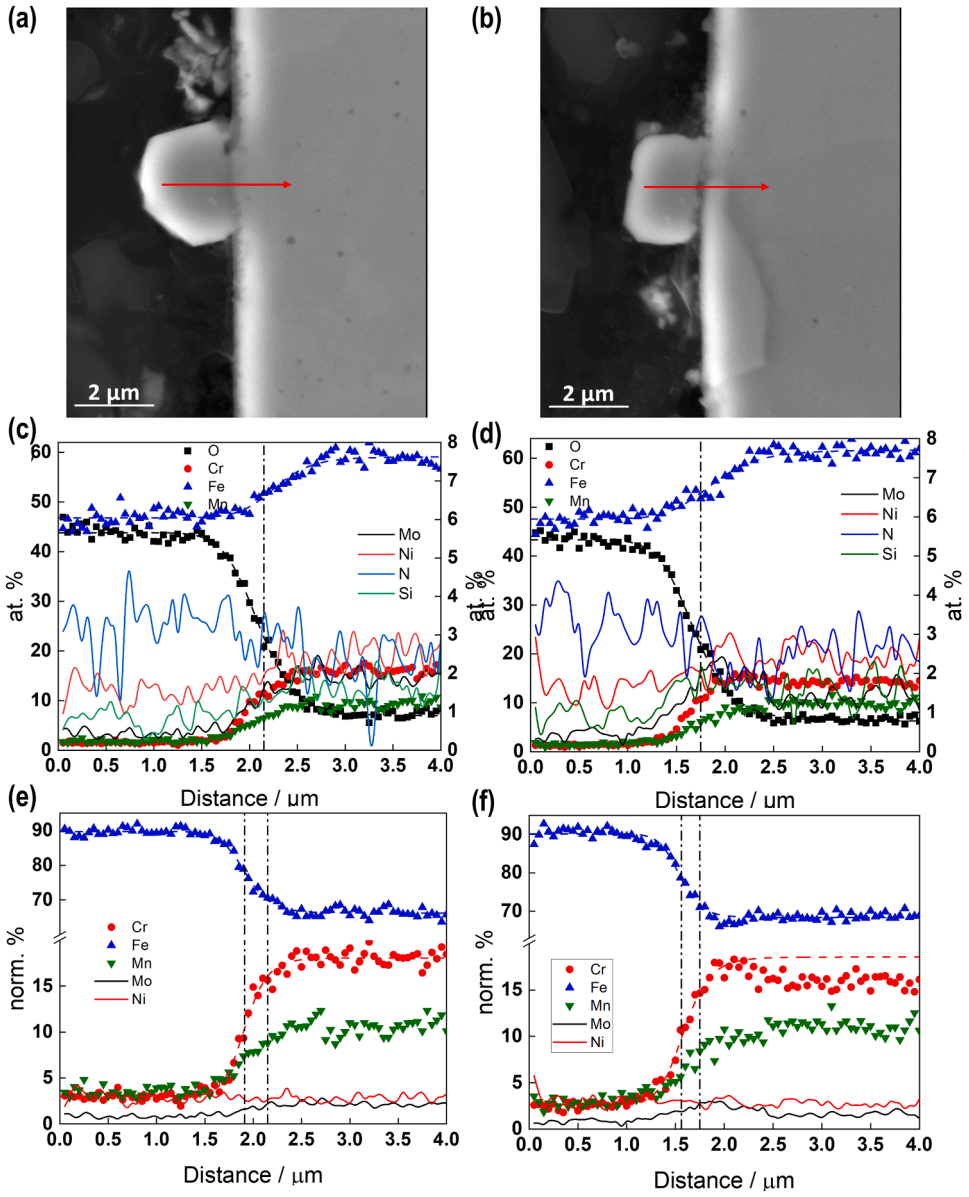

Fig. 12. (a, b) Cross-sectional SEM images (line scan directions are indicated with arrows) and (c-f) EDS line scan results for (a, c, e) High VED and (b, d, f) High VED_HT materials after exposure. (c, d) Atomic concentrations vs. depth, (e, f) normalized cation concentrations vs. depth. Line scan directions are indicated with arrows. Vertical lines indicate the positions of oxide/alloy and outer/inner layer interfaces estimated by sigmoidal fits of depth profiles.

Table 8
Estimated inner and outer layer thicknesses using SEM and EDS line scan results.

Specimen	Outer layer thickness / µm	Inner layer thickness / µm
Low VED	1.53	0.12
Low VED_HT	1.19	0.22
Medium VED	2.15	0.33
Medium VED_HT	1.66	0.37
High VED	1.92	0.27
High VED_HT	1.56	0.21
Ref. 316 L [21]	0.43	0.42

PBF-LB/M nickel-free steels have similar or slightly lower oxidation rate at the alloy/barrier layer interface and diffusion coefficients of oxygen and cations. The present results indicate that the PBF-LB/M produced nickel-free stainless steels are suitable for critical applications in demanding (elevated-temperature) water-based environments such as steam turbines power generation systems, pipelines, pressure vessels and aggressive chemical or renewable industries.

After HT, the nickel-free steels exhibit duplexed phase structures in the heat-treated condition, where the coarse ferritic grains are surrounded by fine austenitic grains and Chi duplex grains. These inhomogeneous barriers contain a high density of grain and phase boundaries, which could slow down the diffusion, transport and oxidation during exposure in corrosive environments. Further investigations into the stress corrosion cracking susceptibility and long-term oxidation behavior of the PBF-LB/M nickel-free steels are needed.

5. Conclusions

The microstructure and high-temperature electrochemical behavior of PBF-LB/M processed Ni-free stainless steel were investigated. The following conclusions can be drawn:

- The PBF-LB/M nickel-free steels processed with various printing parameters and post isothermal heat treatment can exhibit tunable microstructures with high strength.

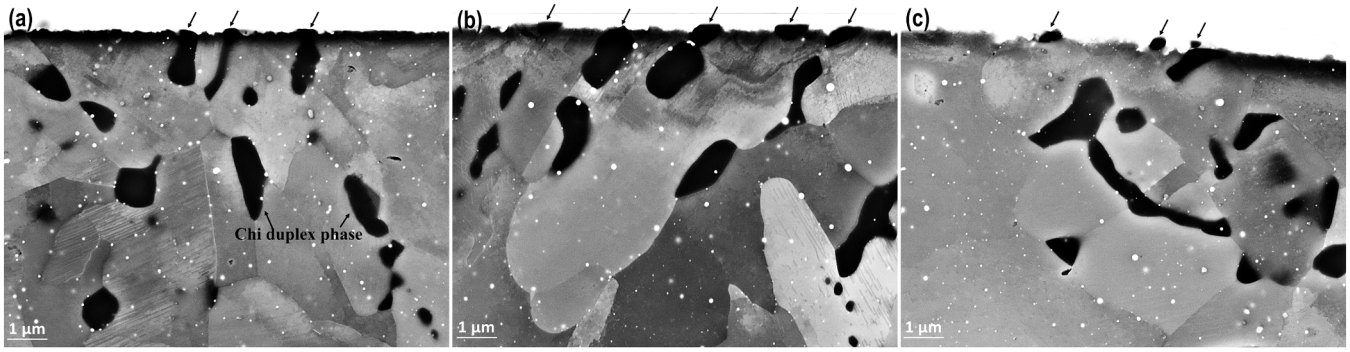

Fig. 13. Cross-sectional SEM BSE images of (a) Low VED_HT, (b) Medium VED_HT and (c) High VED_HT samples after exposure in PWR environment.

- EIS results and their modelling indicate that rate constants of oxidation at the alloy/barrier layer interface (k_M and k_O) are 2–3 times lower for the nickel-free steels when compared to wrought AISI 316 L, and so are the diffusion coefficients of both oxygen and cations. In addition, the field strength in the barrier layer ($\vec{E}$) on Ni-free materials is ca. 50 % higher and barrier layer thicknesses 20 % lower. Accordingly, lower oxidation and corrosion release rates are measured on nickel-free steels in comparison to wrought 316 L.
- Voltammetric measurements and potentiostatic transients do not indicate significant differences between the investigated materials, since these methods do not have sufficient diagnostic power to distinguish individual reaction steps in the complex corrosion mechanism of austenitic alloys.
- Oxide layer characterization indicates important differences between the films on nickel-free steels when compared to AISI 316 L, namely, the composition of the outer layer crystallites is close to a pure Fe oxide, indicating that Mn is most probably preferentially dissolved in the PWR coolant, whereas some amount of Mn is retained in the inner layer. The significantly lower concentration of Ni in the inner oxide and at the alloy/oxide interface could account for the important variations of the parameters of water reduction/hydrogen oxidation reactions with respect to wrought 316 L material.
- The tailored microstructure of PBF-LB/M nickel-free steels exhibit high resistance to corrosion, which are promising for application in demanding environments.

CRediT authorship contribution statement

Ashish Ganvir: Writing – review & editing, Investigation, Formal analysis, Data curation, Conceptualization. **Malte Blankenburg:** Methodology, Investigation, Data curation. **Antti Salminen:** Methodology, Conceptualization. **Tuomas Kantonen:** Methodology, Investigation, Conceptualization. **Efthymios Polatidis:** Writing – review & editing, Methodology, Investigation, Conceptualization. **Timo Saario:** Writing – review & editing, Methodology, Investigation, Formal analysis, Data curation, Conceptualization. **Jan Capek:** Writing – review & editing, Methodology, Investigation, Formal analysis, Data curation, Conceptualization. **Martin Bojinov:** Writing – review & editing, Writing – original draft, Methodology, Investigation, Formal analysis, Data curation, Conceptualization. **Sneha Goel:** Writing – original draft, Methodology, Investigation, Data curation, Conceptualization. **Zaiqing Que:** Writing – review & editing, Writing – original draft, Resources, Project administration, Methodology, Investigation, Formal analysis, Data curation, Conceptualization.

Declaration of Competing Interest

The authors declare that they have no known competing financial interests or personal relationships that could have appeared to influence the work reported in this paper.

Data Availability

Data will be made available on request.

Acknowledgements

SG, TS and ZQ acknowledge the funding from the Euratom research and training program 2014–2018 under grant agreement No. 945300, European Union – NextGenerationEU and the support from the European Union Horizon 2020 research and innovation program under grant agreement no. 857470. MB acknowledges funding from National Recovery and Resilience Plan of the Republic of Bulgaria (Grant No. BG-RRP-2.004-0002 “BiOrgaMCT”). TK, AS and AG acknowledge the funding support from Tenure-Track grant to Prof. Ganvir by University of Turku; Department of Mechanical and Materials Engineering for supporting the MSc thesis of Mr. Tuomas Kantonen and Research Council of Finland as well as European Council for co-funded M.ERANET 2022, GREEN-BAT (2022-2025) project. JC thanks the financial support from the Strategic Focus Area Advanced Manufacturing (SFA-AM) initiative of the ETH Board. The authors would further like to express their gratitude for the helpful discussions and experimental contributions from Aki Toivonen, Tiina Ikäläinen, Johanna Lukin and Taru Lehtikuusi of VTT.

Appendix

According to the Mixed-Conduction Model, if both oxide layer formation/dissolution and dissolution of metals through the oxide (“corrosion release”) are taken into consideration for a spinel-type oxide film (M_3O_4), the following reactions occur at the interfaces:

$$\begin{aligned}
&(\mathrm{M/F})\mathrm{m}\xrightarrow{\mathrm{k_M}}\mathrm{M}_i^{\bullet\bullet}+2\mathrm{e}'\\
&(\mathrm{M/F})\mathrm{m}\xrightarrow{\mathrm{k_O}}3\mathrm{M_M(M_3O_4)}+4\mathrm{V}_\mathrm{O}^{\bullet\bullet}(\mathrm{M_3O_4})+8\mathrm{e}'\\
&(\mathrm{F/S})\mathrm{M}_i^{\bullet\bullet}\xrightarrow{\mathrm{k_{2M}}}\mathrm{M}_{\mathrm{aq}}^{y+}+\left(y-2\right)\mathrm{e}'\\
&\left(\mathrm{F/S}\right)4\mathrm{H_2O}+4\mathrm{V}_\mathrm{O}^{\bullet\bullet}(\mathrm{M_3O_4})\xrightarrow{\mathrm{k_{2O}}}4\mathrm{O_O(M_3O_4)}+8\mathrm{H}^+
\end{aligned}\tag{3}$$

where m is an atom (Fe, Cr, Ni) in the alloy, and the other symbols are consistent with a Kroger-Vink notation (M_M and O_O are normal cation and oxygen positions, $M_i^{\bullet\bullet}$is an interstitial cation, $V_O^{\bullet\bullet}$an oxygen vacancy, and M_{aq}^{y+}a cation in the solution). The interfacial steps are coupled *via* transport of oxygen vacancies and interstitial cations through the barrier part of the oxide, assumed to be governed by diffusion and migration. Consequently, the transfer function to describe the impedance spectra is:

$$Z = R_{el} + Z_{F/S} + Z_f \tag{4}$$

The process at the film/solution interface is most probably dominated by the water reduction-hydrogen oxidation reaction that is assumed to obey a Volmer-Heyrovsky mechanism:

$$\mathrm{H_2O+e^-}\underset{\mathrm{k_{-1H}}}{\overset{\mathrm{k_{1H}}}{\rightleftarrows}}\mathrm{H_{ad}}(\theta)+\mathrm{OH^-}\qquad \mathrm{H_{ad}}(\theta)+\mathrm{H_2O+e^-}\underset{\mathrm{k_{-2H}}}{\overset{\mathrm{k_{2H}}}{\rightleftarrows}}\mathrm{H_2+OH^-}\tag{5}$$

where θ is the surface coverage with atomic hydrogen (H_{ad}). If the rate constants of the respective steps depend exponentially on applied potential:

$$k_i = k_i^0\exp(\pm b_i E), \mathrm{b}_i = \alpha_i\frac{F}{RT}, i = 1H, -1H, 2H, -2H, 2M, 2O \tag{6}$$

the impedance of the film/solution interface is obtained as a small amplitude ac solution of equations:

$$Z_{F/S} = \frac{1}{R_{F/S}^{-1}+\frac{AX}{k_{-2H}c_{H_2}+k_{1H}+k_{-1H}+k_{2H}+j\omega\beta}+j\omega C_{F/S}} \tag{7}$$

The relationships between parameters $R_{F/S}$, A, X, Z_A and the reaction rate constants are given by the expressions:

$$\begin{aligned}
&R_{F/S}^{-1} = F(k_{-1H}b_{-1H}+k_{2H}b_{2H})\overline{\theta}+F(k_{2H}b_{2H}c_{H_2}+k_{1H}b_{1H}+(y-2)k_{2M}b_{2M})(1-\overline{\theta})\\
&\overline{\theta} = \frac{k_{-2H}c_{H_2}+k_{1H}}{k_{-2H}c_{H_2}+k_{1H}+k_{-1H}+k_{2H}},\ A = F(k_{1H}+k_{-1H}-k_{-2H}c_{H_2}-k_{2M}-k_2)\\
&X = k_{-2H}b_{-2H}c_{H_2}-(k_{-2H}b_{-2H}c_{H_2}-k_{1H}b_{1H}+k_{-1H}b_{-1H}-k_{2H}b_{2H})\overline{\theta}-k_{1H}b_{1H}
\end{aligned}\tag{8}$$

Further, the impedance of the oxide film is represented as a parallel combination of the impedance of its electronic properties, Z_e, and two ionic transport impedances pertinent to oxygen vacancies ($Z_{ion,O}$) and interstitial cations ($Z_{ion,M}$), respectively:

$$Z_f = \left(Z_e^{-1}+Z_{ion,O}^{-1}++Z_{ion,M}^{-1}\right)^{-1} \tag{9}$$

The explicit expressions for these impedances are given as:

$$Z_e \approx \frac{RT}{2j\omega F\vec{E}LC_{sc}}\ln\frac{[1+j\omega\rho_d\varepsilon\varepsilon_0\exp(2KL)]}{1+j\omega\rho_d\varepsilon\varepsilon_0}, K = \frac{F}{RT}\vec{E}, \rho_d = \frac{RT}{F^2D_e}\frac{k_{2O}+k_{2M}}{k_O+k_M} \tag{10}$$

$$Z_{ion,O} \approx \frac{RT}{4F^2k_O\left(1-\alpha\right)\left(1+\sqrt{1+\frac{4j\omega}{D_OK^2}}\right)}, Z_{ion,M} \approx \frac{RT}{4F^2k_M\left(1-\alpha\right)\left(1+\sqrt{1+\frac{4j\omega}{D_MK^2}}\right)} \tag{11}$$

where D_e, D_O and D_M are the diffusion coefficients of electronic carriers, oxygen vacancies and interstitial cations, L the thickness of the barrier part of the oxide layer, $\vec{E}$ the field strength in that barrier part, ε the dielectric constant and α the potential consumed in the barrier part at the film/solution interface.

Appendix A. Supporting information

Supplementary data associated with this article can be found in the online version at doi:10.1016/j.corsci.2024.112410.

References

[1] D.D. Gu, W. Meiners, K. Wissenbach, R. Poprawe, Laser additive manufacturing of metallic components: materials, processes and mechanisms, Int. Mater. Rev. 57 (3) (2012) 133–164.

[2] G.M. Mudd, Global trends and environmental issues in nickel mining: Sulfides versus laterites, Ore Geol. Rev. 38 (1–2) (2010) 9–26.

[3] J.J. Hostynek, H.I. Maibach, S.T. Nedorost. Nickel and the Skin: Absorption, Immunology, Epidemiology, and Clinical Aspects, 5th ed., CRC Press, 2003. ⟨https://www.theallergyshop.com.au/assets/files/Nickel⟩ (and the Skin.pdf).

[4] L. Patnaik, S.R. Maity, S. Kumar, Status of nickel free stainless steel in biomedical field: a review of last 10 years and what else can be done, Mater. Today Proc. 26 (2020) 638–643.

[5] K. Yang, Y. Ren, Nickel-free austenitic stainless steels for medical applications, Sci. Technol. Adv. Mater. 11 (1) (2010) 014105.
[6] Q. Wang, Y. Ren, C. Yao, K. Yang, R.D.K. Misra, Residual ferrite and relationship between composition and microstructure in high-nitrogen austenitic stainless steels, Metall. Mater. Trans. A Phys. Metall. Mater. Sci. 46 (2015) 5537–5545.
[7] R.L. Klueh, P.J. Maziasz, E.H. Lee, Manganese as an austenite stabilizer in Fe Cr Mn C steels, Mater. Sci. Eng. A 102 (1988) 115–124.
[8] A.H. Bott, F.B. Pickering, G.J. Butterworth, Development of high manganese high nitrogen low activation austenitic stainless steels, J. Nucl. Mater. 141–143 (1986) 1088–1096.
[9] A.F. Padilha, V. Randle, I.F. Machado, Microstructure and microtexture changes during solution nitriding to produce austenitic case on ferritic–austenitic duplex stainless steel, Mater. Sci. Technol. 15 (1999) 1015–1018.
[10] M.O. Speidel, Nitrogen containing austenitic stainless steels, Materwiss. Werksttech. 37 (10) (2006) 875–880.
[11] A. Hemmasian Ettefagh, S. Guo, J. Raush, Corrosion performance of additively manufactured stainless steel parts: a review, Addit. Manuf. 37 (2021) 101689.
[12] A. Arabi-Hashemi, X. Maeder, R. Figi, C. Schreiner, S. Griffiths, C. Leinenbach, 3D magnetic patterning in additive manufacturing via site-specific in-situ alloy modification, Appl. Mater. Today 18 (2020) 100512.
[13] C. Yang, Q. Wang, Y. Ren, D. Jin, D. Liu, M. Moradi, X. Chen, et al., Corrosion behavior of high nitrogen nickel-free austenitic stainless steel in the presence of artificial saliva and Streptococcus mutans, Bioelectrochemistry 142 (2021) 107940.
[14] M. Talha, C.K. Behera, O.P. Sinha, A review on nickel-free nitrogen containing austenitic stainless steels for biomedical applications, Mater. Sci. Eng. C. 33 (2013) 3563–3575.
[15] S. Xu, F. Gao, J. Han, S. Xiong, X. Duan, F. Zha, B. Yu, L. Yang, Y. Qiao, Z. Zheng, J. Chen, Corrosion Behaviors of Fe-22Cr-16Mn-0.55N High-Nitrogen Austenitic Stainless Steel in 3.5% NaCl Solution. Coatings 12 (2022) 1769.
[16] F. Gao, Y. Qiao, J. Chen, L. Yang, H. Zhou, L. Zh. Zheng, Zhang, Effect of nitrogen content on corrosion behavior of high-nitrogen austenitic stainless steel, npj Mater. Degrad. 7 (2023) 75.
[17] Y. Qiao, X. Wang, J. Chen, L. Yang, X. Wang, H. Zhou, J. Zou, Effect of nitrogen content on corrosion behavior of high-nitrogen austenitic stainless steel, Arab. J. Sci. Eng. 47 (2022) 887–894.
[18] V.B. Vukkum, R.K. Gupta, Review on corrosion performance of laser powder-bed fusion printed 316L stainless steel: Effect of processing parameters, manufacturing defects, post-processing, feedstock, and microstructure, Mater. Des. 221 (2022) 110874.
[19] G. Ko, W. Kim, K. Kwon, T.-K. Lee, The corrosion of stainless steel made by additive manufacturing: a review, Metals 11 (3) (2021) 516.
[20] G.R. Speich, V.A. Demarest, R.L. Miller, Formation of austenite during intercritical annealing of dual-phase steels, Metall. Trans. A Phys. Metall. Mater. Sci. 12 A (1981) 1419–1428.
[21] Z. Que, L. Chang, T. Saario, M. Bojinov, Localised electrochemical processes on laser powder bed fused 316 stainless steel with various heat treatments in high-temperature water, Addit. Manuf. 60 (2022) 103205.
[22] S.E. Ziemniak, M. Hanson, Corrosion behavior of 304 stainless steel in high temperature, hydrogenated water, Corros. Sci. 44 (2002) 2209–2230.
[23] M. da Cunha Belo, M. Walls, N. Hakiki, J. Corset, E. Picquenard, G. Sagon, D. Noel, Composition, structure and properties of the oxide films formed on the stainless steel 316L in a primary type PWR environment, Corros. Sci. 40 (1998) 447–463.
[24] S.E. Ziemniak, M. Hanson, P.C. Sander, Electropolishing effects on corrosion behavior of 304 stainless steel in high temperature, hydrogenated water, Corros. Sci. 50 (2008) 2465–2477.
[25] M. Stern, A.L. Geary, Electrochemical polarization I. A theoretical analysis of the shape of polarization curves, J. Electrochem. Soc. 104 (1957) 56–63.
[26] Z. Que, L. Chang, T. Saario, M. Bojinov, Localised electrochemical processes on laser powder bed fused 316 stainless steel with various heat treatments in high-temperature water, Addit. Manuf. 60 (2022) 103205.
[27] E.-A. Cho, C.-K. Kim, J.-S. Kim, H.-S. Kwon, Quantitative analysis of re-passivation kinetics of ferritic stainless steels based on the high field ion conduction model, Electrochim. Acta 45 (2000) 1933–1942.
[28] J.W. Elmer, S.M. Allen, T.W. Eagar, Microstructural development during solidification of stainless steel alloys, Metall. Trans. A 20 (10) (1989) 2117–2131.
[29] T. DebRoy, H.L. Wei, J.S. Zuback, T. Mukherjee, J.W. Elmer, J.O. Milewski, A. M. Beese, et al., Additive manufacturing of metallic components – process, structure and properties, Prog. Mater. Sci. 92 (2018) 112–224.
[30] P.D. Southwick, R.W.K. Honeycombe, Decomposition of ferrite to austenite in 26% Cr-5%Ni stainless steel, Met. Sci. 14 (7) (1980) 253–261.
[31] Hb Li, Zh Jiang, Zr Zhang, Y. Yang, Effect of grain size on mechanical properties of nickel-free high nitrogen austenitic stainless steel, J. Iron Steel Res. Int. 16 (2009) 58–61.
[32] A.T. Olanipekun, M. Nthabiseng, O.O. Ayodele, M.R. Mphahlele, B.M. Mampuya, P.A. Olubambi, Datasets on the measurement of mechanical properties of ferrite and austenite constitutive phases using nanoindentation and micro hardness techniques, Data Br. 27 (2019) 104551.
[33] J. Mola, E.J. Seo, L. Cho, Correlation between mechanical stability and hardness of austenite in martensite/austenite mixtures, Mater. Sci. Eng. A 822 (Aug. 2021) 141687.
[34] A.T. AlMotasem, M. Posselt, J. Bergström, Nanoindentation and nanoscratching of a ferrite/austenite iron bi-crystal: An atomistic study, Tribol. Int. 127 (2018) 231–239.
[35] E.Y. Guo, H.X. Xie, S.S. Singh, A. Kirubanandham, T. Jing, N. Chawla, Mechanical characterization of microconstituents in a cast duplex stainless steel by micropillar compression, Mater. Sci. Eng. A 598 (2014) 98–105.
[36] S. Chen, G. Ma, G. Wu, A. Godfrey, T. Huang, X. Huang, Strengthening mechanisms in selective laser melted 316L stainless steel, Mater. Sci. Eng. A 832 (2022) 142434.
[37] Soon-Hyeok Jeon, Hye-Jin Kim, Yong-Soo Park, Effects of inclusions on the precipitation of chi phases and intergranular corrosion resistance of hyper duplex stainless steel, Corros. Sci. Vol. 87 (2014) 1–5.
[38] Joanna Michalska, Maria Sozańska, Qualitative and quantitative analysis of σ and χ phases in 2205 duplex stainless steel, Mater. Charact. Vol. 56 (4–5) (2006) 355–362.
[39] A. Di Schino, M. Barteri, J.M. Kenny, Effects of grain size on the properties of a low nickel austenitic stainless steel, J. Mater. Sci. 38 (23) (2003) 4725–4733.
[40] Y. Ge, L. Chang, M. Bojinov, T. Saario, Z. Que, Mechanistic understanding of the localized corrosion behavior of laser powder bed fused 316L stainless steel in pressurized water reactor primary water, Scr. Mater. vol. 238 (115764) (2024).
[41] M. Bojinov, T. Saario, Y. Ge, L. Chang, Z. Que, Effect of hydrogen on electrochemical behavior of additively manufactured 316L in pressurized water reactor primary water, Corros. Sci. vol. 224 (111557) (2023).
[42] M. Bojinov, L. Chang, T. Saario, Z. Que, Corrosion of 316L stainless steel produced by laser powder bed fusion and powder metallurgy in pressurized water reactor primary coolant, Materialia vol. 34 (102055) (2024).